

RESEARCH ARTICLE

Open Access



# Petrogenetic history and melt inclusion characteristics of mantle plume-derived ijolites from NE India: implications for multistage crystallization and occurrence of “nano-calciocarbonatites”

Shubham Choudhary<sup>1</sup>, Koushik Sen<sup>1\*</sup>, Shruti Rana<sup>1</sup> and Santosh Kumar<sup>2</sup>

## Abstract

The Sung Valley ultramafic–alkaline–carbonatite complex (UACC) of Meghalaya, NE, India, is a result of magmatic activity related to the Kerguelen mantle plume spanning from 101 to 115 Ma. In the present study, an integrated crystal size distribution (CSD), mineral chemistry, and melt inclusion analysis are carried out on the ijolites present within this UACC. The CSD analysis shows that these ijolites were formed in multiple stages through changes in the crystallization environment, such as cooling and nucleation rates. Raman spectroscopy of mineral inclusions of rutile, aphtitalite, apatite, carbonate–silicate melt inclusions, and disordered graphite within clinopyroxene and titanite, respectively, indicates a heterogeneous composition of the parental magma. These mineral and melt inclusion phases further suggest localized changes in oxygen fugacity ( $fO_2$ ) due to redox reactions in the lower crust. SEM–EDX analysis of the exposed melt inclusions reveals the presence of alkali-bearing diopside, phlogopite, and andradite, along with an unidentified carbonated silicate daughter phase. The studied melt inclusions are dominated by carbonate, whereas silicates are subordinate. The presence of this fully crystallized carbonate–silicate melt as calcite, diopside, phlogopite, magnetite, apatite, and andradite suggests the presence of “nano-calciocarbonatites” in these ijolites. Our study provides insights into different mechanisms of the loss of alkalis from initially entrapped alkaline carbonate melt in clinopyroxenes. The predominant occurrence of calcite as the only carbonate phase in the studied melt inclusions is a result of silicate–carbonate melt immiscibility, calcite–normative system in these inclusions, dealkalinization of the alkaline carbonates in the presence of external fluid, and/or redistribution of the alkalis to the daughter alkali-bearing silicates.

**Keywords:** Melt inclusions, Raman spectroscopy, Crystal size distribution, Kerguelen plume, Ijolite, Sung Valley

## 1 Introduction

Ijolites are common alkaline rocks composed predominantly of nepheline (30–70 modal %) and clinopyroxene (~40 modal %), mainly diopside and aegirine-augite.

They typically occur as intrusions associated with the ultramafic and carbonatite rocks in various ultramafic-alkaline-carbonatite complexes (UACC) (Gomes *et al.* 2011; Savard and Mitchell 2021). Their global occurrence in several igneous complexes and modes of formation are explained through various magmatic processes. Generally, ijolites are derived either from alkaline magma formed by partial melting of mantle source (Shastry and Kumar 1996), nephelinitic melts derived from the

\*Correspondence: [koushik.geol@gmail.com](mailto:koushik.geol@gmail.com)

<sup>1</sup> Wadia Institute of Himalayan Geology, 33, GMS Road, Dehradun 248001, India

Full list of author information is available at the end of the article

enriched mantle (EM1 and EM2)/metasomatized lithospheric mantle source (Beccaluva et al. 2017; Chmyz et al. 2017; Zhou et al. 2018), or magmas derived from mixing of the mantle and crustal fluids (Nadeau et al. 2016). Numerous studies have been conducted to explain the petrogenetic link between alkaline silicate rocks (i.e., ijolites) and carbonatites that originate from the mantle (e.g., Bell et al. 1998; Winter 2001; Halama et al. 2005; Yaxley et al. 2022). Some authors suggested that the association between these carbonatite and silicate rocks could be attributed to fractional crystallization from a CO<sub>2</sub>-rich parent silicate melt (Watkinson and Wyllie 1971; Lee and Wyllie 1994; Korobeinikov et al. 1998; Nielsen and Veksler 2002; Ulmer and Sweeney 2002; Yaxley et al. 2021). Others favor immiscible separation from a carbonate-bearing silicate melt (Verwoerd 1978; Freestone and Hamilton 1980; Kjarsgaard and Hamilton 1988; Veksler et al. 1998; Halama et al. 2005; Andreeva et al. 2007; Brooker and Kjarsgaard 2011; Guzmics et al. 2012; Sekisova et al. 2015; Stoppa et al. 2019; Chayka et al. 2021; Yaxley et al. 2022). Based on different proxies, the silicate–carbonate immiscibility process has been proposed for various global occurrences, e.g., the Gardiner complex, Greenland (Nielsen 1980; Veksler et al. 1998), the Maoniuping complex, China (Xu et al. 2004), Grønødal-Åka, Greenland (Taubald et al. 2004; Halama et al. 2005) and Kerimasi, Tanzania (Guzmics et al. 2011).

A complete petrogenetic history of igneous rocks also involves the physical history of crystallization, which is recorded by the textures of igneous rocks and explained through crystal size distribution (CSD) analysis. Quantitative textural measurements such as CSD allow direct assessment of the crystallization history of the minerals constituting the igneous rocks. Processes related to crystallizing magmas, such as magma rheology, fractionation, mixing, and cooling, can be very well explained by the CSD analysis (Jaeger 1968; Marsh 1988; Cashman and Marsh 1988; Armenti et al. 1994; Higgins 2000; Klein et al. 2018). CSD gives deep insights into the crystallization processes through the observed textural changes governed by the magma chamber's mechanical processes (Higgins 2011). The slope of the CSD curve helps to understand different processes during the crystallization of magma batches (Marsh 1988). A quantitative measure of the gain or loss of the crystals over a particular size range can also be explained through these CSD curves, which may be useful in evaluating the importance of physical processes such as crystal accumulation and fractionation in a petrologic system (Cashman and Marsh 1988; Marsh 1988).

The physical and chemical evolution of the crystallizing minerals during magmatic processes can also be understood with the help of mineral chemical studies combined

with quantitative measurements such as CSD. Therefore, the chemical composition of minerals and trapped melt inclusions are also equally important in order to construct a thorough petrogenetic record of igneous rocks. Melt inclusions in the crystals are the pockets of parental melt trapped during the crystal growth (Faure and Tisandier 2014). These inclusions not only represent the characteristics of the magma from which their host crystals grew (Anderson 1979; Roedder 1979; Sobolev 1996; Frezzotti 2001; Danyushevsky et al. 2002; Guzmics et al. 2008, 2011; Mitchell 2009) but also record evolving melt compositions and physicochemical conditions prevailing during crystallization (Roedder 1972). Carbonate–silicate melt inclusions serve as a powerful tool to assess the paragenetic relationship among silicate and carbonate rocks of alkaline–carbonatite complexes (Andreeva et al. 2007). These carbonate melts also work as effective agents for the transportation of rare earth and alkaline earth elements (Guzmics et al. 2009; Mitchell 2009). The alkali-rich composition of carbonate–silicate melt inclusions in alkaline–carbonatite rocks places them very close to the representation of the actual parental magma composition that these rocks crystallize from (Nielsen et al. 1997; Sokolov et al. 1999; Yaxley et al. 2022). The investigation of these melt inclusions of alkaline rocks (ijolites) becomes even more crucial while assessing the petrogenetic relationship among alkaline–carbonatite rocks, such as liquid immiscibility during crystallization of their parental magmas (Guzmics et al. 2012; Chayka et al. 2021; Berkesi et al. 2020).

In the northeastern part of India, ijolites are exposed in the Sung Valley UACC, along with ultramafic rocks and carbonatites. Previous geochemical and stable and radiogenic isotopic studies suggest that these different suites of rocks from Sung Valley UACC are not co-genetic (Ray and Pande 2001; Srivastava and Sinha 2004; Srivastava et al. 2005). In the present work, we integrated crystal size distribution, mineral chemistry, and melt inclusions studies to explain a complete sequence of formation of Sung Valley ijolites from their petrogenetic conditions to crystallization history along with the nature of parental magma and history of melts involved. Our results suggest that these ijolites crystallized in multiple stages and had some petrogenetic relation with associated carbonatites. The composition of the trapped melt inclusions in these rocks must have changed significantly during syn- to late-magmatic processes.

## 2 Geological background

The oval-shaped ultramafic-alkaline–carbonatite complex (UACC) of Sung Valley is hosted by the Shillong Plateau of Meghalaya in northeastern India (Fig. 1a, b). The Sung Valley UACC is related to the Kerguelen plume (Veena

et al. 1998; Ray et al. 1999, 2000; Srivastava and Sinha 2004; Srivastava et al. 2005; Srivastava 2020). This UACC intrudes the Archean gneiss, schist, and the Proterozoic Shillong Group rocks in the Shillong Plateau (Ray and Pande 2001). The Sung Valley UACC and several other alkaline intrusive bodies are hosted by the N–S trending Um Ngot lineament, which is genetically related to the Ninety-East Ridge in the Indian Ocean (Gupta and Sen 1988). The Sung Valley UACC crystallized within the age range of 101–115 Ma (Ray and Pande 2001; Srivastava and Sinha 2004; Srivastava et al. 2005, 2019). This UACC is composed of ultramafic, alkaline, and carbonatite rocks. Ijolites occur as a ring dyke in the Sung Valley UACC, whereas the melilitolite, nepheline syenite, and carbonatites that occur as oval-shaped bodies and small dykes within the pyroxenite and peridotite/serpentinized peridotites (Fig. 1b). Sung Valley pyroxenites are dominantly clinopyroxene rich and show the presence of chalcopyrite of low-temperature origin as the main sulfide mineral (Choudhary et al. 2022). Carbonatites are exposed mostly in the southern part of the Sung Valley UACC (Srivastava and Sinha 2004). Sung Valley ijolites, the third most abundant rock type after pyroxenites and peridotites, are mostly coarse-grained with wide textural variation from porphyritic to poikilitic. The emplacement date of these Sung Valley ijolites is 115.1 Ma (Srivastava et al. 2005), whereas in situ U–Pb SIMS of perovskite from these ijolites yielded an age of  $104.0 \pm 1.3$  Ma (Srivastava et al. 2019). These ijolites occur as a ring dike and the petrological and geochemical studies carried out in the past suggest that these rocks, along with the associated ultramafic (peridotite and pyroxenite) and carbonatite rocks, are formed from the batches of primitive magma with a distinct magmatic affinity such as olivine melilitites, basanites, and carbonatites, and these batches of magma evolved independently (Melluso et al. 2010). These primitive magmas were derived at a pressure greater than 2.5 GPa from a metasomatically enriched carbonated peridotite (Srivastava and Sinha 2004). The whole-rock geochemical characteristics shown by these ijolites are significantly different from nepheline syenite, suggesting that the nepheline syenites are not formed through the fractionation of ijolites (Srivastava and Sinha 2004).

### 3 Methods

#### 3.1 Crystal size distribution

Crystal size distribution (CSD) measurements were performed on clinopyroxene (aegirine-augite and diopside) grains in Sung Valley ijolites. Four representative samples were chosen for the analysis and multiple thin sections of each sample were prepared to obtain a grain count

of 300–400 statistically. A high-resolution petrographic microscope was used to take the photomicrographs of each rock-thin section. Crystal margins were outlined using the vector drafting tool of CorelDraw. Software Image-J was used to analyze the mineral outlines and related parameters of the clinopyroxene crystals, such as area, perimeter, and length. Finally, the CSD of the clinopyroxene crystals was calculated with the program CSD-Corrections 1.6 (Higgins 2000).

#### 3.2 Electron probe micro-analyses (EPMA)

Polished rock thin sections of 0.03 mm thickness were prepared for petrographic and electron microprobe analyses. For mineral chemistry, four representative samples were analyzed using a CAMECA SXFive Electron Probe Micro Analyzer instrument at SERB-IRHPA National Facility, Department of Geology, Banaras Hindu University, India. For quantitative mineral chemistry analyses, wavelength-dispersive spectrometry and a LaB6 source were used. During the analysis, the instrument was operated at an acceleration voltage of 15 kV and focused beam current of 10 nA having a diameter of 1  $\mu\text{m}$ . The following crystals, such as TAP (thallium acid phthalate), LPET (large pentae-rythritol), and LLIF (large lithium fluoride) were used for the measurements. The natural mineral standards such as diopside, forsterite, almandine, albite, and orthoclase supplied by CAMECA-AMETEK were used for calibration and quantification. A precision better than 1% for major element oxides from the repeated analyses of standards was achieved during the analysis. The representative mineral chemical data are given in Tables 2 and 3.

#### 3.3 Raman spectroscopy

The compositions of melt and minute crystals in the untreated inclusions from four representative samples were obtained by laser-excited Raman spectrometry using Horiba Jobin Yvan Lab Ram HR Laser Raman Micro Probe in Raman and Fluid inclusion lab at Wadia Institute of Himalayan Geology (WIHG), Dehradun. All the Raman spectra were generated using 100X objectives and with the 514 nm laser of Argon ion ( $\text{Ar}^+$ ) source with a dispersion of a fixed holographic grating 1800 lines/mm. The laser spot size at the time of analysis was  $\sim 2$   $\mu\text{m}$ . To obtain a better signal-to-noise ratio, repeated spectra were recorded in the 100–4000  $\text{cm}^{-1}$  region. Standard silicon was used for the calibration of the instrument. Raman shift at 520.59  $\text{cm}^{-1}$  during the calibration with standard silicon was achieved. Other parameters during the analyses were taken as follows: acquisition time  $\sim 5$ –15 s, accumulations  $\sim 2$ , and laser power  $\sim 10$  mW.

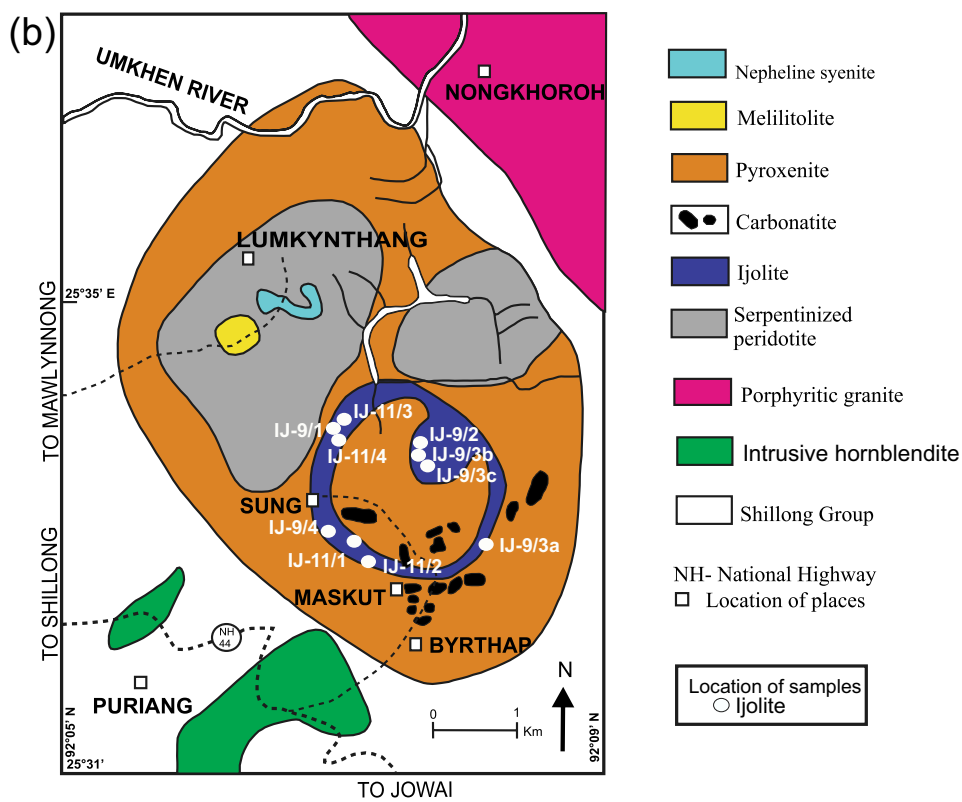
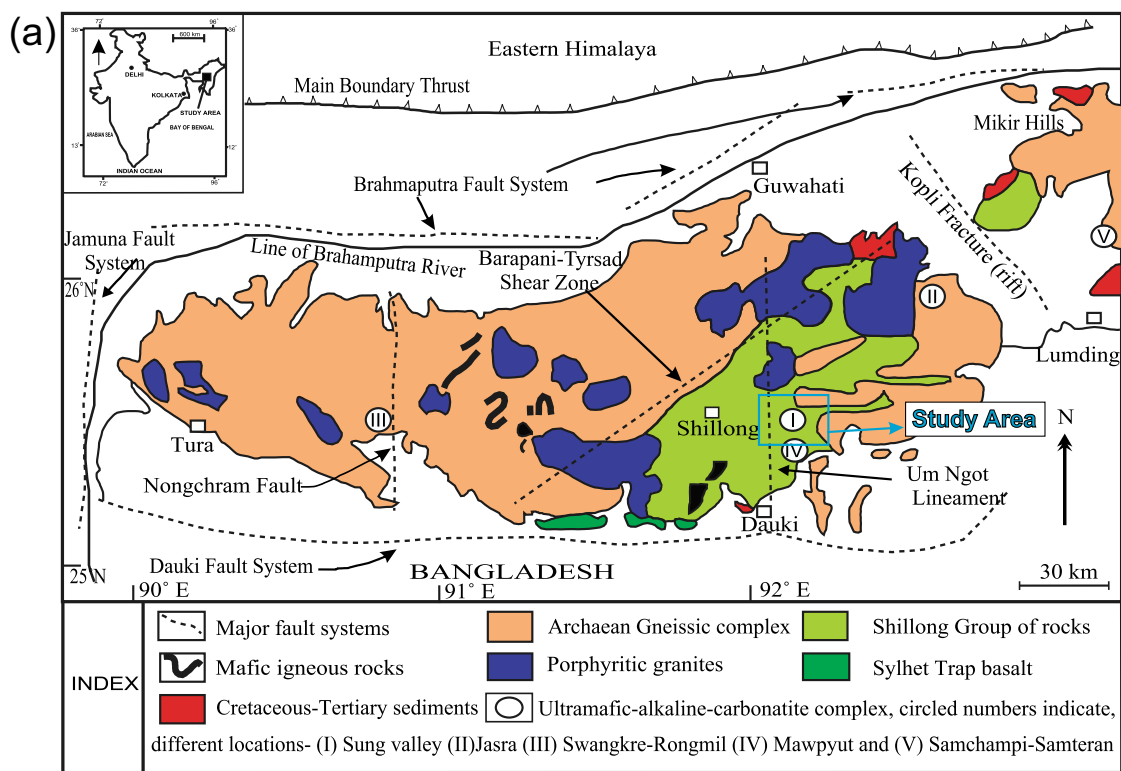


**Fig. 1** Geological maps. **a** Shillong plateau. **b** Sung Valley, Meghalaya, NE India; highlighted with a square in (a). **a, b** Modified after Srivastava and Sinha (2004)

### 3.4 SEM-EDX

Back-scattered electron (BSE) imaging and energy-dispersive X-ray (EDX) qualitative analyses on exposed melt inclusions were acquired using Carl Zeiss SMT EVO 40 Series-Scanning Electron Microscope (SEM) with EDX, equipped with LaB6 cathode, at Wadia Institute of Himalayan Geology, Dehradun. BSE images were acquired using 20 kV accelerating voltage and beam current of 3–6 nA at different magnifications. The concentration of oxides (wt %) of the elements was analyzed by EDS attachment using the QUANTAS software.

## 4 Results

### 4.1 Petrography

A total of ten samples were analyzed in this study. All the fresh ijolite samples were collected from different locations in the Sung Valley UACC (Fig. 1b). Collected ijolite samples are dominantly composed of nepheline and clinopyroxene, mainly aegirine-augite (Aeg-Aug) and diopside (Fig. 2a). These ijolites are medium to coarse-grained and predominantly show hypidiomorphic textures (Fig. 2a, b, d). The poikilitic texture is also present in sample IJ-9/4, where clinopyroxene crystals are enclosed in large optically continuous nepheline crystals (Fig. 2c). The accessory mineral phases include apatite and titanite (Fig. 2b, c, d). Minor opaque minerals include magnetite, pyrite, pyrrhotite, and chalcopyrite (Fig. 2d). The representative mineral chemistry data for the various phases in these ijolites are given in Tables 2 and 3, and the results are detailed in the following subsection.

### 4.2 Crystal size distribution

Four representative samples (IJ-9/2, IJ-11/2, IJ-9/4, and IJ-11/1) were chosen for CSD analysis. The CSD results related to the clinopyroxene (aegirine-augite and diopside) crystals, such as area, perimeter, and length, were imported into the CSDCorrections 1.6 software (Higgins 2000) to make the stereological corrections (Fig. 3). All the calculations were performed assuming a massive fabric with 0.8 roundness on the block-ellipsoid scale. Clinopyroxene crystals contacting the edge of the sample area were not taken into consideration during analysis, as these crystals cannot be representative of complete crystals. The resultant 3D crystal size distributions are given in Table 1. A total of ~1475 clinopyroxene grains were analyzed from the representative samples, and crystal size ranged from microns to millimeter scale (Table 1). The crystal size of clinopyroxene grains ranges from 0.08 to 5.65, 0.12 to 7.5, 0.03 to 1.16, and 0.13 to 9.3 mm in the samples IJ-9/2, IJ-11/2, IJ-9/4, and IJ-11/1, respectively (Table 1). The CSD plots between the natural logarithm of crystal population density  $\ln(n)$  vs. crystal length (mm) in

samples no. IJ-9/2, and IJ-11/1 show a concave upward trend starting with a slight convex upward kink (Fig. 4a, d). Sample no. IJ-11/2 exhibits concave upward CSD (Fig. 4b). The CSD of clinopyroxene in a sample IJ-9/2 shows an inflection point at ~2 mm, whereas sample IJ-11/2 shows inflection points at 2 and 7 mm (Fig. 4a, b). Sample no. IJ-9/4, which exhibits poikilitic texture, shows the most distinct CSD profiles with marked differences in the slope nearly a straight line (Fig. 4c). The studied ijolites do not show any signatures of deformation such as annealing, dislocation, or diffusion of clinopyroxenes (Fig. 2).

### 4.3 Mineral composition

The EPMA was carried out on clinopyroxene and titanite of representative ijolite samples. The chemical analysis of clinopyroxene is given in Table 2. Analyzed clinopyroxene grains include both diopside and aegirine-augite (Fig. 3a). The average end-member composition of these clinopyroxene grains is  $(\text{Di}_{53-84}\text{Hd}_{10-32}\text{Ae}_{4-16})$  (Table 2). Clinopyroxene composition ranges as: MgO from 8.26 to 12.58 wt.%, CaO from 20.68 to 24.28 wt.%,  $\text{FeO}^{\text{t}}$  (as total iron) from 6.78 to 14.37 wt.%,  $\text{Na}_2\text{O}$  from 0.47 to 1.88 wt.%, and  $\text{SiO}_2$  from 48.46 to 51.32 wt.%. The Mg# of clinopyroxene varies from 62.5 to 89.77 (Table 2). In terms of International Mineralogical Association (IMA) recommended Q-J parameters (Morimoto et al. 1988), which are based on six oxygens, the analyzed clinopyroxene spots (Table 2) largely belong to jadeite-free quadrilateral pyroxene (Fig. 3b). The Q-J plot shows that these clinopyroxenes are crystallized at low-pressure conditions possibly at crustal depth. Mg# in clinopyroxene shows a positive correlation with Ti content (Fig. 3c). The clinopyroxene in studied ijolites show enrichment in diopside and to some extent, hedenbergite but are low in aegirine content, which shows that these are unevolved compared to the clinopyroxene in ijolites from Kerimasi and Fen complex (Fig. 3a) (Church 1996; Mitchell 1980; Káldos et al. 2015). These characteristics, such as almost jadeite-free composition and low aegirine content of clinopyroxene from studied ijolites, suggest that these are early crystallizing phases (Fig. 3a, c) (Káldos et al. 2015). The composition of titanite such as CaO varies from 26.88 to 27.89,  $\text{TiO}_2$  from 36.15 to 38.14,  $\text{FeO}^{\text{t}}$  from 1.04 to 1.60, and  $\text{SiO}_2$  from 29.51 to 30.15 wt.% (Table 3). A minor amount of trace elements oxides was also observed, such as  $\text{La}_2\text{O}_3$  ranging from 0.02 to 0.17 and  $\text{Nb}_2\text{O}_5$  from 0.44 to 1.07 wt.% (Table 3). Fe/Al ratios (>0.5) in the studied titanite (Table 3) point toward their derivation from silica-undersaturated magma forming plutonic rocks such as



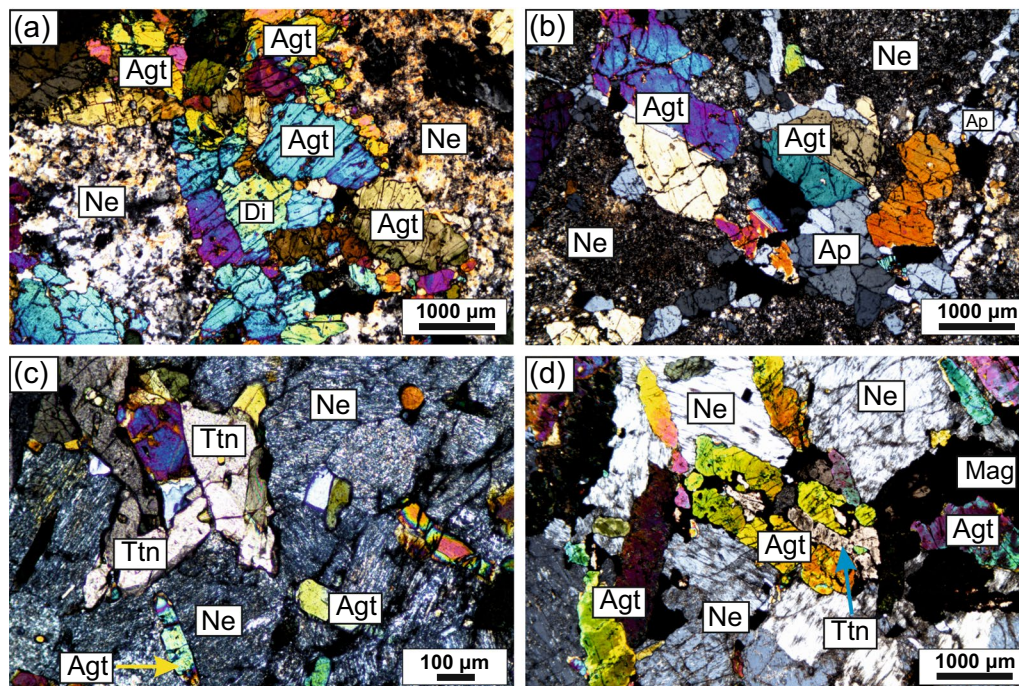


**Fig. 2** Petrographical photomicrographs of representative samples from Sung Valley ijolites in cross-polarized light. **a** Subhedral diopside, aegirine-augite, and nepheline forming the hypidiomorphic texture. **b** Subhedral to anhedral aegirine-augite showing simple twinning along with the apatite and nepheline. **c** Aegirine-augite enclosed by nepheline with subhedral to anhedral titanite crystals forming the poikilitic texture. **d** Subhedral aegirine-augite, titanite, nepheline, and magnetite showing hypidiomorphic texture. *Aeg-Aug* Aegirine-augite; *Di* Diopside; *Ne* Nepheline; *Ap* Apatite; *Ttn* Titanite; *Mag* Magnetite

Sung Valley ijolites in the present case (Kowallis et al. 2022).

#### 4.4 Melt inclusions and mineral inclusions petrography

A diverse population of ~90 melt inclusions, hosted by clinopyroxene (diopside and aegirine-augite) and titanite, was observed in the same four samples, which were used for CSD analysis of Sung Valley ijolites. These melt inclusions were recognized from transmitted light microscopy during melt inclusion petrography (Fig. 5). Most of the melt inclusions are elongated oval in shape ranging between 2 and 15  $\mu\text{m}$  in size (Fig. 5c, e, f). Some are irregular and rounded to subrounded ranging from 3 to 6  $\mu\text{m}$  in size (Fig. 5g, h). One sample IJ-9/2, also hosts some monophase mineral inclusions along with the melt inclusions in clinopyroxene (Fig. 5d). Melt and mineral inclusions hosted by titanite, were also observed in one sample IJ-9/4 (Fig. 5a, b). Mineral inclusions in titanite are granular in appearance and of rhombus shape ranging from 2 to 8  $\mu\text{m}$  in size (Fig. 5a). These inclusions occur in a secondary trail, which terminates right at the boundary of titanite crystal (Roedder 1979). Melt inclusions hosted by titanite in the same sample IJ-9/4 are irregular to subrounded with 2–5  $\mu\text{m}$  in size (Fig. 5b). Melt inclusions in

clinopyroxene and titanite typically show some distorted/deformed shrinkage bubbles probably compressed to the wall in the inclusions. This also is a typical behavior of carbonatite-type melt inclusions (Golovin et al. 2020). However, most of the clinopyroxene-hosted melt inclusions contain cavities instead of shrinkage bubbles. The absence of any decrepitation haloes in the melt inclusions suggests that the original compositions of trapped phases are intact and not altered due to any change in ambient pressure conditions after entrapment (Fig. 5). Melt inclusions observed in clinopyroxenes are present in the cores of these grains, which suggests that they are essentially primary. However, many of them could also be secondary in nature as they distinctly form linear and planar alignments within the crystals (Fig. 5). Despite being hosted by the cores of the crystals, these inclusions might have been entrapped at the intermediate stage of the minerals' growth. BSE images of melt inclusions do not show any bubbles (Fig. 6). However, the empty cavities could possibly be representing the places of the former fluid phase, which probably existed earlier in these melt inclusions and escaped during exposure. High-resolution BSE images of the melt inclusions show the presence of subhedral to euhedral daughter crystals that are 2 to 10  $\mu\text{m}$

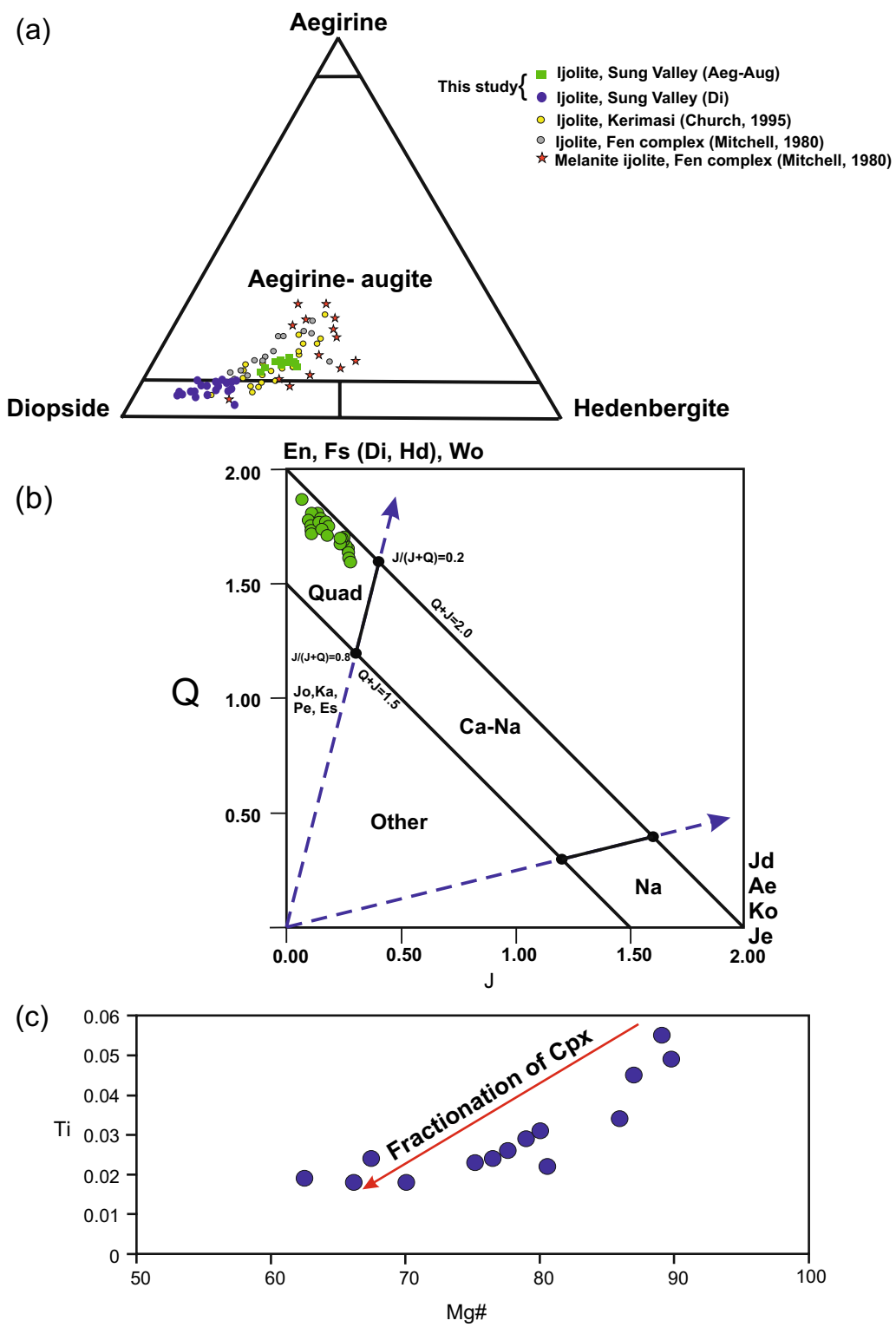


**Fig. 3** Plots related to the chemistry of clinopyroxene crystals in Sung Valley ijolites. **a** Triangular Na-Mg-Fe classification diagram showing that all points of mineral chemistry of clinopyroxene fall in the area diopside and aegirine-augite. This figure also shows the comparison of clinopyroxene from ijolites in Sung Valley UACC with clinopyroxene from Kerimasi and Fen complex ijolites. **b** Q-J classification diagram for the pyroxenes (Morimoto et al., 1988) showing that all the points of clinopyroxene (aegirine-augite and diopside) composition fall into the Quad field. **c** Scatter plot between Mg# and Ti in Clinopyroxene showing the depletion of Ti along the line of fractionation of Clinopyroxene

**Table 1** Crystal size distribution (CSD) of Cpx of ijolites in the Sung Valley UACC

Mineral	Sample	Area (mm <sup>2</sup> )	Total grains	Length size (mm) for area measured	
				(Minimum)	(Maximum)
Cpx	IJ-9/2	1007.13	437	0.0843	5.653
Cpx	IJ-11/2	1003.25	300	0.12	7.5
Cpx	IJ-9/4	1930.46	368	0.0346	1.1675
Cpx	IJ-11/1	1683.88	370	0.1309	9.3993

in size in these melt inclusions (Fig. 6). A significant space of the melt inclusions is occupied by these daughter crystals (Fig. 6). A very limited variation in volume proportion displayed by the crystals in these melt inclusions

testifies that these are daughter minerals and not accidentally trapped minerals (Fig. 6) (Anderson et al. 2003).

**4.5 Raman spectroscopy of the mineral and melt inclusions**

Raman Spectroscopy was used to investigate the phase composition of the trapped melt inclusions in clinopyroxene and titanite. Mineral inclusions hosted by titanite in sample IJ-9/4 were identified as calcite, where the Raman spectrum shows characteristic symmetric stretching vibration  $\nu_1$  with a very strong band at 1086.8  $\text{cm}^{-1}$  (Frezzotti et al. 2012) (Fig. 5a). Melt inclusions in titanite in sample IJ-9/4 show that they have calcite accompanied by graphite in the shrinkage bubble, where calcite shows its characteristic symmetric stretching vibration  $\nu_1$  with a very strong band

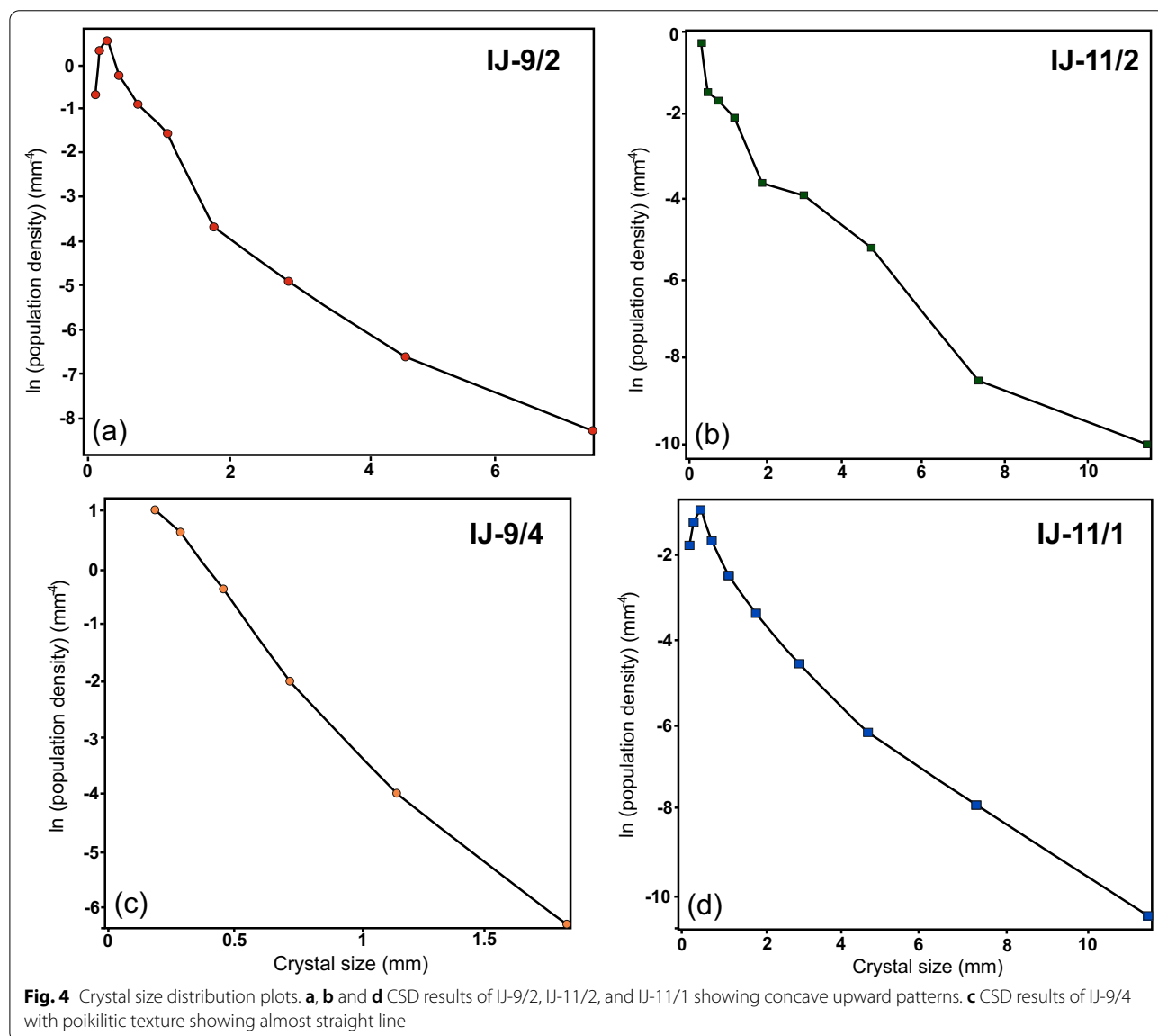




**Table 2** Quantitative mineral chemistry data

	1	2	3	4	5	6	7	8	9	10	11	12	13	14	15
Spot analysis															
SiO <sub>2</sub>	51.32	50.98	50.67	51.07	50.82	51.16	50.3	49.85	48.46	48.29	49.84	50.33	48.61	49.71	47.29
TiO <sub>2</sub>	0.79	1.11	1.01	0.91	0.85	0.8	0.61	1.2	1.59	1.73	0.65	0.62	1.09	0.83	1.92
Al <sub>2</sub> O <sub>3</sub>	1.87	2.24	2.15	1.96	2.24	1.42	1.8	3.08	4.03	4.56	1.77	1.72	2.63	2.24	4.88
FeO	9.17	9.27	9.65	9.87	9.37	9.45	13.9	7.96	7.74	6.78	14.26	12.48	14.37	12.64	6.92
MnO	0.17	0.22	0.16	0.22	0.33	0.39	0.68	0.15	0.13	0.19	0.48	0.58	0.68	0.42	0.15
MgO	12.52	11.77	11.74	11.78	11.34	12.54	8.78	12.58	11.99	12.42	8.64	9.7	8.26	9.11	11.85
CaO	22.82	23.07	22.89	22.67	22.58	23.05	21.09	23.76	23.99	24.28	20.68	21.71	20.86	21.31	24.13
Na <sub>2</sub> O	1.07	1.28	1.19	1.2	1.26	0.47	1.84	0.85	0.83	0.7	1.82	1.64	1.88	1.81	0.74
K <sub>2</sub> O	0.00	0.01	0.00	0.00	0.00	0.02	0.02	0.02	0.03	0.03	0.04	0.02	0.00	0.00	0.02
Total	99.73	99.95	99.46	99.68	98.79	99.30	99.02	99.45	98.79	98.98	98.18	98.80	98.38	98.07	98.00
On the basis of 60															
Si	1.916	1.903	1.903	1.915	1.922	1.931	1.928	1.863	1.825	1.810	1.929	1.923	1.880	1.915	1.795
Ti	0.022	0.031	0.029	0.026	0.024	0.023	0.018	0.034	0.045	0.049	0.019	0.018	0.032	0.024	0.055
Al	0.082	0.099	0.095	0.087	0.100	0.063	0.081	0.136	0.179	0.201	0.081	0.077	0.120	0.102	0.218
Fe <sub>3</sub>	0.118	0.126	0.128	0.120	0.100	0.066	0.165	0.134	0.143	0.133	0.163	0.163	0.198	0.155	0.137
Fe <sub>2</sub>	0.168	0.163	0.175	0.190	0.196	0.233	0.280	0.115	0.101	0.079	0.299	0.236	0.267	0.252	0.082
Mn	0.005	0.007	0.005	0.007	0.011	0.012	0.022	0.005	0.004	0.006	0.016	0.019	0.022	0.014	0.005
Mg	0.697	0.655	0.657	0.658	0.639	0.705	0.502	0.701	0.673	0.694	0.498	0.553	0.476	0.523	0.671
Ca	0.913	0.923	0.921	0.911	0.915	0.932	0.866	0.951	0.968	0.975	0.857	0.889	0.864	0.880	0.981
Na	0.077	0.093	0.087	0.087	0.092	0.034	0.137	0.062	0.061	0.051	0.137	0.122	0.141	0.135	0.054
K	0	0.000	0.000	0.000	0.000	0.001	0.001	0.001	0.001	0.001	0.002	0.001	0.000	0.000	0.001
Sum	4.00	4.00	4.00	4.00	4.00	4.00	4.00	4.00	4.00	4.00	4.00	4.00	4.00	4.00	4.00
Mg#	80.57	80.04	78.99	77.61	76.49	75.19	66.16	85.94	86.99	89.77	62.50	70.08	64.08	67.47	89.07

The table shows the composition of Cpx (Diopside and Aegirine-Augite) based on EPMA point analysis

at 1085.4 cm<sup>-1</sup> and very weak (vw) band at 854.5 cm<sup>-1</sup> (Frezzotti et al. 2012) and disordered graphite shows its characteristic D and G Raman bands at 1351 and 1578.5 cm<sup>-1</sup>, respectively (Das et al. 2017) (Fig. 5b). Special care was taken during the recording of Raman spectra of graphite to make sure that the D and G bands do not appear due to burning of the sample wafer by laser. So all the spectra of graphite were recorded using lesser laser power. Furthermore, to avoid any contamination due to carbon coated on the samples during EPMA, separate wafers of the samples were used during Raman spectroscopy. Asterisks in Raman spectra are assigned to the host peaks of titanite (Fig. 5a, b). The carbonate component in the melt inclusions hosted by clinopyroxene in this sample (IJ-9/4) was also identified as calcite, which again shows a very sharp peak at 1086.5 cm<sup>-1</sup> showing symmetric stretching vibration  $\nu_1$  with a very strong band, strong (s) band at 157 cm<sup>-1</sup>, and medium weak (mw) band at 713 cm<sup>-1</sup> (Fig. 5c) (Frezzotti et al. 2012). The presence of apatite in the studied melt inclusions was also confirmed where the Raman spectrum shows a very strong band at 964 cm<sup>-1</sup> (Fig. 5c). Mineral inclusions hosted by clinopyroxene in

sample IJ-9/2 were identified as rutile showing its very strong (vs) bands at 443 cm<sup>-1</sup> and 609.5 cm<sup>-1</sup> (Frezzotti et al. 2012) (Fig. 5d). The carbonate component in melt inclusions in this sample (IJ-9/2) and two other samples IJ-11/1 and IJ-11/2 also showed symmetric stretching vibration  $\nu_1$  at, 1085.7, 1086 and 1085.4 cm<sup>-1</sup>, respectively, which were identified as calcite (Frezzotti et al. 2012) (Fig. 5e-g). Melt inclusions hosted by clinopyroxene in sample IJ-11/2 were identified as containing apatite (K-Na sulfate), showing its very strong band at 985.6 cm<sup>-1</sup>, medium band at 448 cm<sup>-1</sup> along with the CO<sub>2</sub> showing two bands of Fermi doublet at 1278.4 and 1384 cm<sup>-1</sup> (Frezzotti et al. 2012) (Fig. 5h). Host clinopyroxene in all the samples shows strong Raman bands at ~ 1010 and 667 cm<sup>-1</sup> (Thompson et al. 2005). It is worth noting that during the Raman spectroscopy of these melt inclusions, the spectra of glass were not detected. However, in the present case, it is reasonable because the carbonatitic melts cannot be quenched to a glass (owing to very low viscosity) and inevitably crystallize (Moine et al. 2004; Giuliani et al. 2012; Kamenetsky et al. 2014; Chayka et al. 2021). All the Raman

**Table 3** Quantitative mineral chemistry data

	1	2	3	4	5	6	7	8	9	10	11	12	13	14	15
Spot analysis															
SiO <sub>2</sub>	29.73	29.60	29.80	30.15	29.96	30.06	30.11	29.89	29.51	30.02	29.94	29.58	29.92	30.08	29.77
TiO <sub>2</sub>	38.14	37.72	36.92	36.71	37.11	36.87	37.29	36.70	37.11	37.13	36.46	37.26	36.15	37.19	37.20
Al <sub>2</sub> O <sub>3</sub>	0.50	0.53	0.78	0.72	0.51	0.55	0.54	0.71	0.50	0.57	1.07	0.67	0.66	0.59	0.70
FeO	1.22	1.36	1.44	1.51	1.25	1.04	1.18	1.33	1.20	1.11	1.45	1.13	1.60	1.20	1.38
MnO	0.00	0.00	0.00	0.00	0.00	0.00	0.00	0.00	0.00	0.00	0.00	0.00	0.00	0.00	0.00
MgO	0.00	0.00	0.00	0.00	0.00	0.00	0.00	0.00	0.00	0.00	0.00	0.00	0.00	0.00	0.00
CaO	26.88	27.55	27.83	27.46	27.76	27.89	27.25	27.63	27.52	27.14	26.93	27.23	27.31	27.85	27.50
La <sub>2</sub> O <sub>3</sub>	0.02	0.07	0.00	0.06	0.17	0.16	0.11	0.23	0.14	0.04	0.06	0.09	0.14	0.00	0.05
Nb <sub>2</sub> O <sub>5</sub>	0.76	0.73	0.56	0.62	0.56	0.74	0.98	1.07	0.94	0.63	0.64	0.67	0.44	0.54	0.66
Total	97.25	97.56	97.32	97.22	97.31	97.32	97.47	97.56	97.00	96.60	96.50	96.63	96.22	97.45	97.25
On the basis of 50															
Si	1	1	1	1	1.01	1.02	1.02	1.01	1	1.02	1.02	1	1.02	1.01	1.01
Ti	0.97	0.96	0.94	0.93	0.94	0.94	0.95	0.93	0.95	0.95	0.93	0.95	0.93	0.94	0.94
Al	0.01	0.02	0.03	0.02	0.02	0.02	0.02	0.02	0.02	0.02	0.04	0.02	0.02	0.02	0.02
Fe <sub>2</sub>	0.03	0.03	0.04	0.04	0.03	0.02	0.03	0.03	0.03	0.03	0.04	0.03	0.04	0.03	0.03
Mn	0	0	0	0	0	0	0	0	0	0	0	0	0	0	0
Mg	0	0	0	0	0	0	0	0	0	0	0	0	0	0	0
Ca	0.97	1	1.01	0.99	1	1.01	0.98	1	1	0.98	0.98	0.99	1	1	0.99
Sum	3.00	3.00	3.00	3.00	3.00	3.00	3.00	3.00	3.00	3.00	3.00	3.00	3.00	3.00	3.00

The table shows the composition of titanite based on EPMA point analysis

spectra of inclusions were acquired repeatedly, and representative spectra are presented in Fig. 5.

#### 4.6 SEM–EDX of the melt inclusions

SEM–EDX analysis was carried out to determine the chemical composition of daughter phases associated with carbonate components in the exposed melt inclusions hosted by clinopyroxene (diopside and aegirine-augite). Points for EDX analysis were selected with the help of BSE images (Fig. 6). Representative oxides data for the daughter phases in studied melt inclusions are given in the Additional file 1: Table S1, and the results are detailed below. The daughter crystals in these carbonate–silicate melt inclusions were identified as phlogopite, andradite garnet, diopside, and magnetite, similar to the phases observed in melt inclusions in ijolites by Andreeva et al. (2007) and Sekisova et al. (2015) (Fig. 6). The chemical composition (oxides wt %) of the most widespread daughter crystals in the studied melt inclusions varies as follows: Andradite shows SiO<sub>2</sub>, 38.49 to 40.69; TiO<sub>2</sub>, 1.50 to 4.92; Al<sub>2</sub>O<sub>3</sub>, 1.02 to 4.93; Fe<sub>2</sub>O<sub>3</sub>, 17.70 to 23.39; MgO, 0.21 to 1.98; CaO, 26.08 to 30.89; Na<sub>2</sub>O, 0.19 to 1.91; K<sub>2</sub>O, 0.21 to 2.85; with a minor amount of F ~ 0.04 and Cl from 0.28 to 1.80. Phlogopite shows SiO<sub>2</sub>, 38.12 to 38.34; TiO<sub>2</sub>, ~ 2.00; Al<sub>2</sub>O<sub>3</sub>, 10.48 to 18.64; Fe<sub>2</sub>O<sub>3</sub>, 5.92 to 8.49; MgO, 20.44 to 22.21; CaO, 1.77 to 3.63; Na<sub>2</sub>O, 2.20 to 3.34; K<sub>2</sub>O, 7.77 to 8.26; with a minor amount of

Cr<sub>2</sub>O<sub>3</sub> ~ 0.57; F ~ 0.01; Cl from 0.12 to 0.33; P<sub>2</sub>O<sub>5</sub> ~ 0.31 and SO<sub>3</sub> from 0.32 to 3.8. It is noteworthy that phlogopite usually does not contain a substantial amount of calcium, and this estimation of CaO could likely be a result of a signal originating from the neighboring phases, such as host clinopyroxene or calcite in the melt inclusions (Fig. 6). Diopside shows SiO<sub>2</sub>, 47.87 to 50.02; TiO<sub>2</sub>, ~ 1.70; Al<sub>2</sub>O<sub>3</sub>, 0.79 to 1.97; Fe<sub>2</sub>O<sub>3</sub>, 3.01 to 3.91; MgO, 11.20 to 14.87; CaO, 20.37 to 22.38; Na<sub>2</sub>O, 5.78 to 7.38; K<sub>2</sub>O, 2.43 to 3.66; with a minor amount of Cr<sub>2</sub>O<sub>3</sub> ~ 1.46; F, 0.03 to 0.07; Cl from 0.35 to 0.89; P<sub>2</sub>O<sub>5</sub>, 0.75 to 0.80 and SO<sub>3</sub> from 0.46 to 0.45. Similarly, diopside also may not contain ~ 5 to 7% Na<sub>2</sub>O like omphacite, which is certainly not possible to occur in these ijolites. Neither can it have 2 to 3% K<sub>2</sub>O, which is only likely in ultra-high-pressure clinopyroxene. We infer that these signals may also be coming from the phlogopite in these melt inclusions due to contamination from the neighboring phase (Fig. 6). Magnetite shows TiO<sub>2</sub>, 4.51; Al<sub>2</sub>O<sub>3</sub>, 0.20; Fe<sub>2</sub>O<sub>3</sub>, 87.11; MnO, 2.29; MgO, 1.29 and Cr<sub>2</sub>O<sub>3</sub>, 4.54 (Additional file 1: Table S1). Additionally, one carbonated silicate phase was also analyzed with the unusual chemical composition varying as: SiO<sub>2</sub>, 16.91; Al<sub>2</sub>O<sub>3</sub>, 6.38; Fe<sub>2</sub>O<sub>3</sub>, 21.82; MgO, 9.05; CaO, 29.14; Na<sub>2</sub>O, 4.55; and K<sub>2</sub>O, 6.12; with a minor amount of F, 0.02; Cl, 1.95; P<sub>2</sub>O<sub>5</sub>, 0.98; and SO<sub>3</sub>, 3.06 (Additional file: Table S1). Raman spectroscopy and SEM-EDX studies indicate that the studied melt

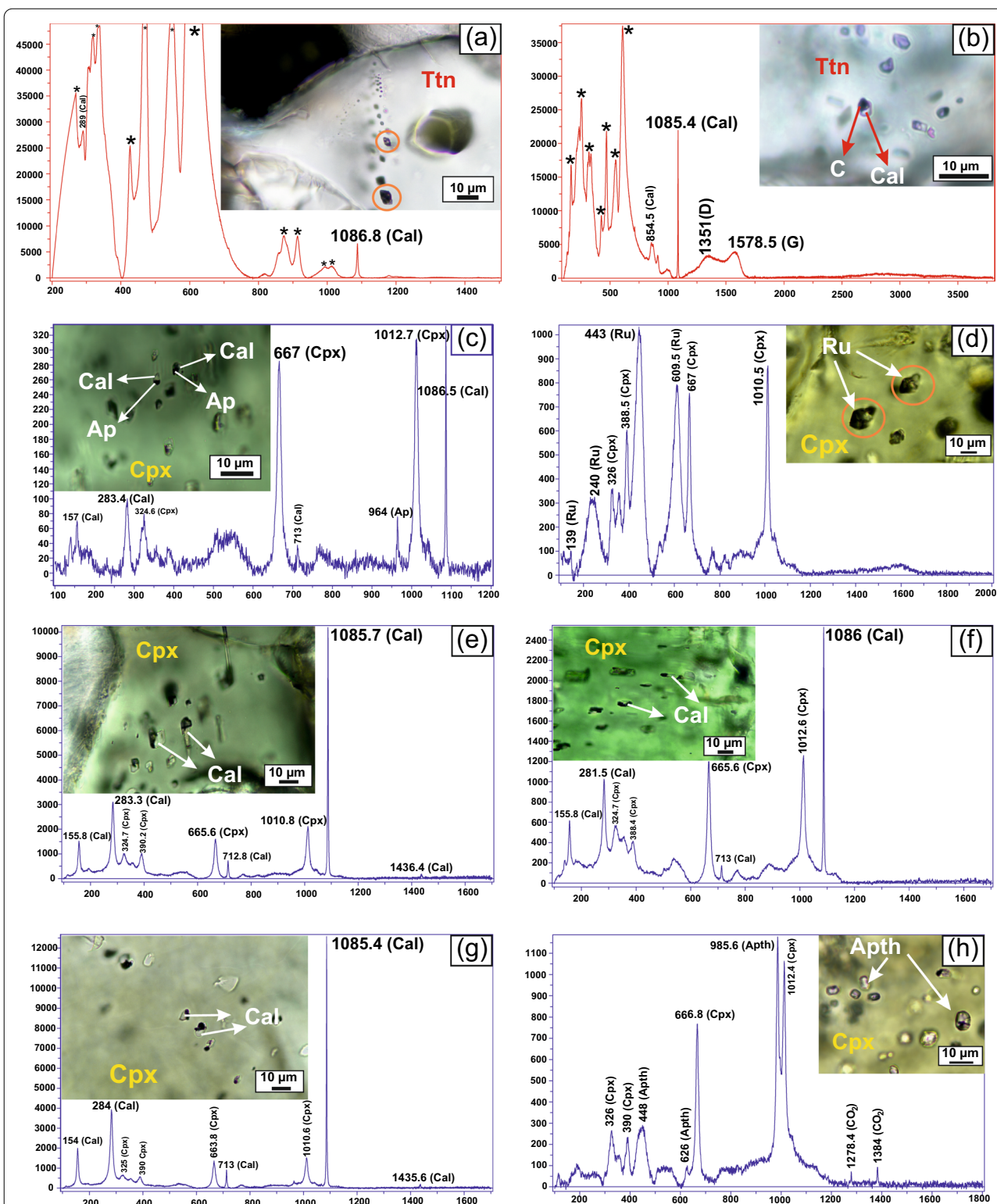


**Fig. 5** Photomicrographs and Raman spectra of melt inclusions. **a** Secondary mineral inclusions trail hosted by titanite in sample IJ-9/4 showing calcite. **b** Melt inclusions in titanite in IJ-9/4 showing the presence of calcite in glass and graphite in shrinkage bubble (Asterisks show the Raman peaks of host titanite). **c** Calcite and apatite in melt inclusions hosted by clinopyroxene in IJ-9/4. **d** Presence of rutile in mineral inclusions hosted by clinopyroxene in IJ-9/2. **e, f and g** Melt inclusions hosted by clinopyroxene in IJ-9/2, IJ-11/1, and IJ-11/2 showing the presence of calcite in Raman spectrum. **h** Apophthalite and CO<sub>2</sub> in melt inclusions. [All the Raman spectra show Raman shift (cm<sup>-1</sup>) on x-axis and Intensity (cnt) on y-axis.] Orange circles around the inclusions show mineral inclusions, while the rest of all are the melt inclusions. *Aeg-Aug* Aegirine-augite, *Ap* Apatite, *Ttn* Titanite

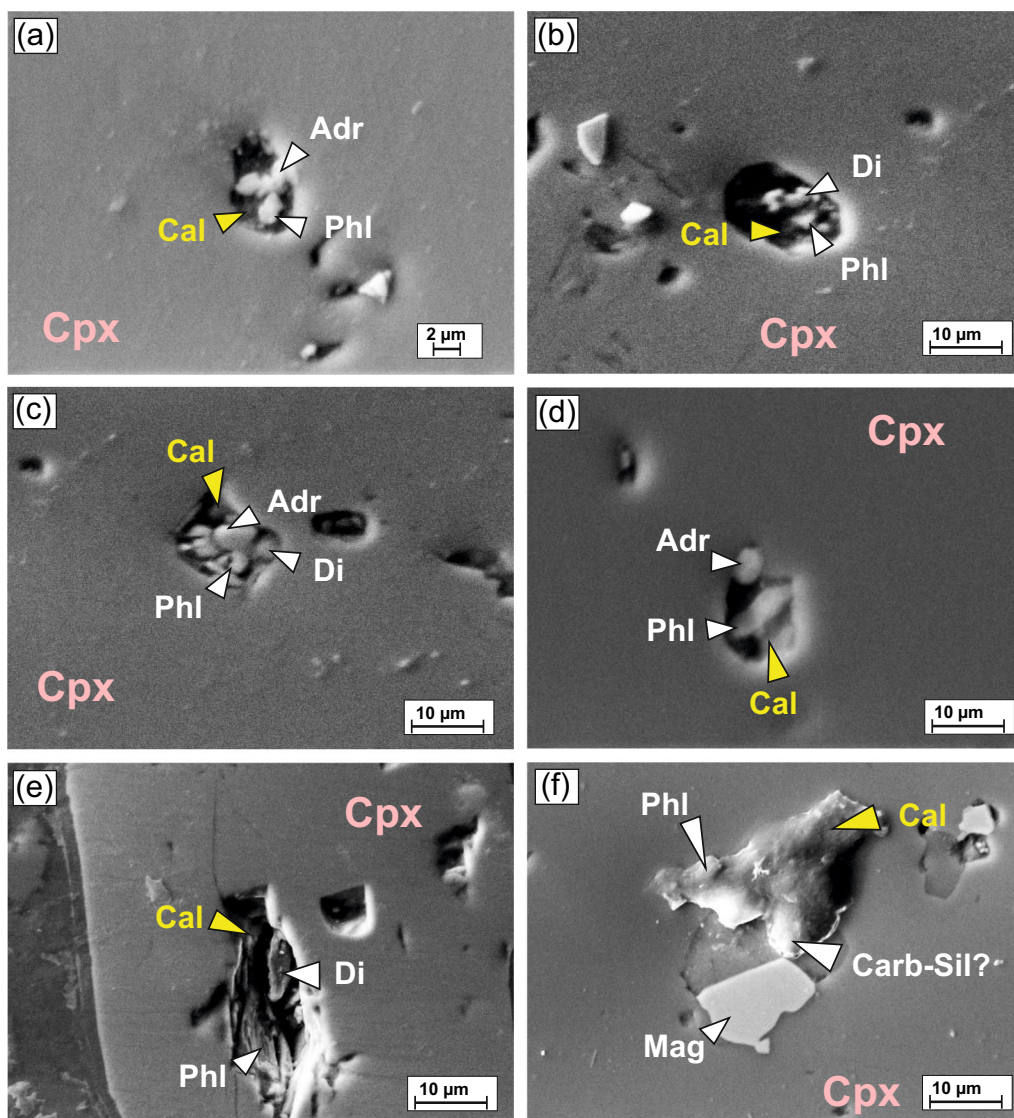


**Fig. 6** BSE images of the exposed carbonate–silicate melt inclusions in clinopyroxene from Sung Valley ijolites. BSE images showing the presence of alkali-bearing diopside, phlogopite, andradite, magnetite, and carbonated silicate daughter crystals with calcite. *Di* Diopside, *Phl* Phlogopite, *Adr* Andradite, *Mag* Magnetite

inclusions are dominated by carbonates, whereas silicates are subordinate (Fig. 5, 6). This further confirms that the parental melt for the inclusions was carbonatitic with silicate component (Golovin et al. 2018, 2020). Also, the fact that these inclusions are consistently made up of a variety of crystals of different phases is the key evidence that they are not just mineral inclusions, which are most commonly monophasic, but rather represent aliquots of trapped liquid that crystallized within these melt inclusions (Fig. 5, 6). The quantitative EDX data of the analyzed phases are not significantly contaminated by the

host as there are almost no alkalis in the host as shown by mineral chemistry data (Table 2), whereas we have a significant amount of alkalis in the daughter phases (Additional file 1: Table S1). Therefore, the studied inclusions are carbonate–silicate (carbonatite-like) melt inclusions (Figs. 5, 6). Based upon the Raman spectroscopy and SEM–EDX data and by virtue of the occurrence of typical liquidus phases of calcio-carbonatitic liquids, i.e., calcite, apatite, diopside, phlogopite, garnet, and magnetite as a fully crystallized melt, these melt inclusions can also be termed as “nano-calcio-carbonatites” (Figs. 5, 6).



## 5 Discussion

### 5.1 Crystallization history of Sung Valley ijolites

A complete absence of annealing, dislocation, and diffusion in these clinopyroxenes rules out any possibility of post-magmatic recrystallization (Fig. 2). Therefore, the textural parameters observed during CSD analysis are unaffected by any sub-solidus processes and they represent the primary magmatic character (Fig. 4). All the CSDs of the analyzed samples show curved concave upward distribution (Fig. 4). Hence, a single population model of crystals cannot be applied. There can be various inferences based upon curved CSDs that can result from the crystallization in igneous systems. We will discuss all possible interpretations in the context of our CSD dataset (Fig. 4; Table 1) for the Sung Valley ijolites.

The first explanation for the curved CSD can be the crystal fractionation process (Marsh 1998). However, this possibility can be negated because curved CSDs that result due to the crystal fractionation process show nearly the same intercepts in CSD plots (Higgins 1996). On the contrary, in the present case, all the CSD plots show different intercepts (Fig. 4). The second explanation can be the change in growth rate as a function of crystal size, where growth rate increases with the size of crystals (Marsh 1988; Eberl et al. 2002). This argument can also be negated because a curved but concave downward CSD pattern can result through this process, as explained by Inanli and Huff (2009), unlike concave upward CSD in the present study (Fig. 4). Additionally, the cases of such variable crystal growth rates with size have not been described yet in the geological environments (Higgins 1996). The third possible explanation for producing curved CSDs can be the magma-mixing hypothesis (Higgins 1996), where melts of different compositions interact physically and chemically, which leads to the disequilibrium condition giving rise to partial resorption e.g., corona texture in clinopyroxene. A complete absence of any such texture (Fig. 2) in the present study further negates this possibility. The fourth possible explanation that can produce the concave upward CSDs is fines destruction (Marsh 1988). In this process, larger crystals are more likely to remain at depth, whereas the small crystals rise at shallower levels in the magma chamber and are resorbed (Higgins 2002). During the fines destruction process, nutrients of the resorbed smaller crystals are fed to the larger crystals (Higgins 1996, 2011). The abundance of large crystals of clinopyroxene compared to smaller ones also suggests that crystal growth rate dominated over the nucleation along with the simultaneous dissolution of smaller clinopyroxene crystals (Fig. 4). Such coarsening in the CSD data, which is also substantiated with petrography (Fig. 2), may have a bearing on the high-temperature magmatic storage. Fifth and

the last possible explanation to give rise to the curved CSDs with kinks is the abrupt changes in the crystallization environment e.g., cooling rate (Marsh 1988; Armienti et al. 1994), which can also control the nucleation rate (Kamacı and Altunkaynak 2019). This inference is further supported by the similar composition of both the smaller and larger clinopyroxene crystals of Sung Valley ijolites (Table 2), which can be related to the modification of the crystallization environment without any significant changes in the composition of these crystals in the present case (Higgins 2011). The last two possible explanations seem to best fit in the context of observed curved concave upward CSDs in Sung Valley ijolites (Fig. 4). Furthermore, changes in the crystallization environment (cooling rate, nucleation, and growth rate) can incorporate mixed crystals of different generations, which in turn can give rise to concave upward CSD (Morgan et al. 2007). The clinopyroxene CSD in the Sung Valley ijolites can be separated into two categories, where samples IJ-9/2, IJ-11/2, and IJ-11/1 (Fig. 4a, b, d) show curves with inflection points, whereas sample IJ-9/4 (Fig. 4c) displays nearly a straight line. These observations suggest that clinopyroxene in IJ-9/4 grew in a single stage, and in the rest of the samples IJ-9/2, IJ-11/2 and IJ-11/1, these crystals grew in multiple stages (Wang et al. 2019) (Fig. 4).

### 5.2 Petrogenetic conditions of Sung Valley ijolites: existing models

The Sung Valley UACC rocks are derived from the partial melt of carbonated peridotite at a pressure greater than 2.5 GPa (Srivastava and Sinha 2004; Srivastava et al. 2005). Geochemical studies of the different rock units from the Sung Valley UACC further suggest that these rocks were formed by discrete batches of primitive magmas with different magmatic affinities, and these magmas probably derived from the same source yet evolved independently (Srivastava et al. 2005; Melluso et al. 2010). On the basis of whole-rock geochemical and isotopic studies, Veena et al. (1998) and Ray et al. (2000) concluded that Sung Valley rocks are formed from partial melting of the subcontinental lithospheric mantle, which was previously subjected to metasomatism by Kerguelen mantle plume-derived fluids. Pieces of evidence of carbonate metasomatism of the lithospheric mantle beneath Sung Valley UACC were recently delineated by Choudhary et al. (2021). Therefore, assuming a carbonated peridotite source to the parental melt of ijolite during partial melting would be appropriate, as also suggested by Srivastava et al. (2005). The mineralogical composition of Sung Valley ijolites corroborates the earlier geochemical studies (e.g., Srivastava and Sinha 2004; Melluso et al. 2010) and suggests that these rocks were formed from a magma of nephelinitic affinity, which was

derived from partial melting of a carbonated peridotite. Srivastava et al. (2005) obtained a high concentration of LREE in chondrite-normalized rare-earth patterns in these ijolites, such concentration of LREEs points toward a low degree of partial melting during the derivation of parental melt to the Sung Valley ijolites. Isotopic studies on Sung Valley ijolites carried out by Ray et al. (1999) suggest that parental magma to these ijolites was derived from either a low U/Pb source or interacted with a low U/Pb mantle reservoir. Our mineral chemical data show a jadeite-free composition of the analyzed clinopyroxene in the present study (Fig. 3b; Table 2), which supports the inference that this melt was crystallized at crustal depth after its origin at greater than 2.5 GPa pressure (Srivastava and Sinha 2004).

### 5.3 Composition of melt inclusions: nature of parental ijolite melt and presence of “nano-calcio-carbonatites”

The carbonate–silicate melt inclusions observed in the present study, as well as the models proposed by earlier studies, suggest that these ijolites were formed from a carbonated olivine-nephelinite magma (Melluso et al. 2010), which was probably derived from partial melting of carbonated peridotite (Srivastava and Sinha 2004). The silica-undersaturated nature of the parental magma of these ijolites is further supported by Fe/Al ratios ( $>0.5$ ) in the titanite (Table 3) (Kowallis et al. 2022). These nano-calcio-carbonatites represent a typical assemblage of liquidus phases that crystallized from calcio-carbonatitic liquid (Figs. 5, 6). The predominant occurrence of carbonate component, i.e., calcite in melt inclusions in the core of these crystals suggests that these carbonates represent the pristine magma and are not derived from carbonate metasomatism of ijolite itself as suggested elsewhere (Seifert and Thomas 1995; Jones et al. 2000; Downes et al. 2002; Woolley and Bailey 2012). An abundance of carbonate–silicate melt inclusions in the Sung Valley ijolites (Figs. 5, 6) also testifies that the source rock is a carbonated peridotite, as suggested by Srivastava and Sinha (2004). The presence of disordered graphite with calcite in titanite of a sample IJ-9/4 (Fig. 5b) and mineral inclusions of rutile in clinopyroxene of sample IJ-9/2 (Fig. 5d), together indicate the fluctuation of  $fO_2$ , invoked by redox reactions in the lower crust during the entrapment of these inclusions (Fig. 5). We opine that during the entrapment of these inclusions, tetravalent  $Ti^{4+}$  cations from the parental magma consumed enough oxygen provided by carbonate–silicate melt (enriched in  $CO_2$ ) to form rutile (Fig. 5d), which in turn reduced the residual  $CO_2$  to graphite (Fig. 5b). The presence of  $CO_2$  can be justified here because the carbonate components of these melts are enriched in  $CO_2$  and  $H_2O$  (Jones et al. 2013; Choudhary et al. 2021). A positive correlation between

Mg# and Ti in clinopyroxene (Fig. 3c) also indicates that Ti is concentrated in the form of rutile inclusions during the early fractionation of the clinopyroxene at high temperature. The Ti content kept decreasing with Mg# along the clinopyroxene fractionation line (Fig. 3c). However, the parental magma of these ijolites got saturated in Ti later, which resulted in the formation of titanite (Fig. 2c, d). The occurrence of apthitalite (K-Na sulfate) (Fig. 5h) in inclusions marks the presence of oxidized S-rich fluid in the crystallizing magma (Bataleva et al. 2018). However, the occurrence of these sulfates is common in carbonate–silicate melts (Chayka et al. 2021).

Melt inclusions can record evidence of liquid immiscibility in magmas from a variety of different tectonic settings (Thompson et al. 2007; Panina and Motorina 2008; Mitchell 2009; Kamenetsky and Kamenetsky 2010; Sekisova et al. 2015). It is noteworthy that the carbonate component in all the carbonate–silicate melt inclusions in clinopyroxene and titanite in the studied ijolites are purely calcite (Figs. 5, 6), and carbonatites associated with these ijolites in the Sung Valley UACC are also purely calcio-carbonatites belonging to the sovitic carbonatite group (Choudhary et al. 2021). Therefore, the first possible explanation of the occurrence of studied melt inclusions can be the separation of carbonate melt from silicate melt or silicate–carbonate melt immiscibility at the waning stages of the formation of the Sung Valley UACC. A number of previous studies on the Sung Valley UACC have also suggested the immiscibility model among silicate and carbonate rocks (Viladkar et al. 1994; Veena et al. 1998; Sen 1999; Ray et al. 2000). However, lower Ba/La ratios in carbonatites in comparison to associated silicate rocks, as well as a paucity of immiscible droplets of carbonate liquid in the associated silicate rocks negated this possibility (Hamilton et al. 1989; Srivastava and Sinha, 2004; Melluso et al., 2010). Moreover, these authors did not completely rule out the immiscibility model and suggested the possibility of the liquid immiscibility of Sung Valley carbonatites from a more primitive liquid. However, a complete absence of any alkali carbonates, such as nyerereite, shortite, and natrite, in the studied melt inclusions questions the possibility of the immiscibility process (Fig. 5). However, calcite being a typical liquidus phase in a carbonatite melt cannot be the only phase resulting from crystallization of such a melt. Although the possibility of silicate–carbonate melt immiscibility cannot be completely ruled out, this calcite discrepancy and loss of alkalis from carbonates need to be addressed through some alternate models.

The second possible explanation for the occurrence of these carbonate and silicate phases can be their accidental entrapment, just as solid crystals in these melt inclusions. However, this process is also unlikely as the ijolites

under investigation are magmatic rocks that are devoid of any post-magmatic recrystallization. Furthermore, a very limited variation in volume proportion in the crystals in these melt inclusions advocates against such a possibility (Fig. 6) (Anderson et al. 2003). Additionally, the occurrence of a variety of these crystals of different phases suggests that they are the aliquots of trapped crystallizing liquid within these melt inclusions (Figs. 5, 6).

The predominant occurrence of calcite as the only carbonate phase also points toward a calcite-normative system in the studied melt inclusions. This could be the third possible explanation and such calcite-normative system of the studied carbonate melts could result through either extreme fractionation of carbonate–silicate melt or continuous infiltration of alkali-poor carbonate melt during the crystallization of clinopyroxenes and initially present alkali-rich carbonate melt. This infiltration process could take place through magmatic metasomatism during syn to late magmatic processes (Mathez 1995).

Generally, the alkali carbonates may undergo a prompt replacement by calcite even at low-temperature (Zaitsev and Keller 2006). During such processes, the leaching of alkalis (e.g., Na, K) takes place from soluble alkali carbonatite liquids through dealcalization with the formation of stable calcite instead (Le Bas 1981; Chen et al. 2013; Chayka et al. 2021). Therefore, the fourth possible explanation could be the dealcalization of the initially trapped alkaline carbonates to calcite. However, this possibility of such dealcalization appears to be controversial in the present case as this process requires an open system for the trapped melt inclusions and also the presence of some external fluid during late-stage crystallization or sub-solidus conditions of these ijolites. Only a single titanite crystal in one sample (IJ-9/4), hosts secondary mineral inclusions of calcite that points toward occurrence of external fluid (Fig. 5a). However, paucity of such secondary inclusions and absence of any sub-solidus processes indicated by CSD analysis (Fig. 4) argue against this possibility. It is noteworthy that sometimes the melt inclusions, appearing as primary, do not behave as an absolutely closed system, but there could still be micro-/nano-fissures through which late- or post-magmatic fluids enter the inclusion and modify their composition. These micro-fissures may be healed again due to solid-state diffusion processes in crystals, leaving no evidence of the alteration event, as similarly reported by Chayka et al. (2020 & 2021). Based on this argument, the process of dealcalization cannot be ruled out completely.

The fifth and last possible scenario for the observed calcite discrepancy in the studied melt inclusions could be the redistribution of alkalis to the coexisting silicate phases within the inclusions, leaving only calcite as a carbonate phase (Fig. 6). The alkali contents of the host

clinopyroxene is very low (Table 2). Therefore, the alkalis from the initial alkaline carbonate melt could be redistributed to the daughter silicate phases inside these carbonate–silicate melt inclusions (Fig. 6). This inference is also supported by the presence of a notable amount of alkalis in the daughter diopside, phlogopite, and the unidentified carbonate–silicate phases (Additional file 1: Table S1). Therefore, it may be plausible that the daughter crystals took up the alkalis from the initial carbonate melt, and calcite was left as the final carbonate phase (Figs. 5, 6). Finally, out of all the possible scenarios, first and the last three seem to be responsible for a predominant occurrence of calcite in these carbonate–silicate melt inclusions or nano-calcio-carbonatites. These melt inclusions in the studied ijolites clearly indicate the activity of complex alkali-bearing carbonate–silicate–phosphate–sulfate melts during the crystallization of these ijolites (Figs. 5, 6).

## 6 Conclusions

Based on the results obtained in this study, the following conclusions can be drawn:

- Sung Valley ijolites dominantly show concave upward CSD patterns caused by the fines destruction process and abrupt changes in the crystallization environment; also, these rocks were crystallized in multiple stages.
- The presence of calcite and alkali silicates in carbonate–silicate melt inclusions in the clinopyroxene points toward silicate–carbonate immiscibility during the formation of Sung Valley ijolites and carbonatites.
- The predominant occurrence of calcite as the only carbonate phase in the studied melt inclusions suggests that these inclusions could also be a result of (i) calcite-normative system in these melts resulting from either extreme fractionation of carbonate–silicate melt or continuous infiltration of alkali-poor carbonate melt, (ii) dealcalization of the initially trapped alkaline carbonates in the presence of external fluid that entered through micro-/nano-fissures which subsequently healed, (iii) redistribution of alkalis to the coexisting silicate phases (diopside, garnet, phlogopite and carbonated silicate) within the inclusions, leaving calcite as the only carbonate phase.

## Abbreviations

Aeg-Aug: Aegirine-augite; Adr: Andradite; BSE: Back-scattered electron; Cal: Calcite; CO<sub>2</sub>: Carbon dioxide; CSD: Crystal size distribution; Di: Diopside; EDX:

Energy-dispersive X-ray; EM1: Enriched mantle 1; EM2: Enriched mantle 2; EPMA: Electron probe micro-analyses;  $fO_2$ : Oxygen fugacity; GPa: Gigapascal; IMA: International Mineralogical Association; LLIF: Large lithium fluoride; LPET: Large pentaerythritol; LREE: Light rare-earth elements; Mag: Magnetite; Mg#: Magnesium number; mw: Medium weak; Phl: Phlogopite; s: Strong; S: Sulfur; SEM: Scanning electron microscope; TAP: Thallium acid phthalate; UACC: Ultramafic–alkaline–carbonatite complex; vs: Very strong; vw: Very weak; WIHG: Wadia Institute of Himalayan Geology.

## Supplementary Information

The online version contains supplementary material available at <https://doi.org/10.1186/s40645-022-00531-1>.

**Additional file 1.** Representative oxides data for the daughter phases in studied melt inclusions obtained through SEMEDX analysis.

## Acknowledgements

The authors thank the Director, WIHG, Dehradun, for encouragement and support. Prof. N. V. Chalapathi Rao, Department of Geology, Banaras Hindu University (BHU), is thanked for carrying out the microprobe analyses at SERB-IRHPA-sponsored EPMA laboratory. N. K. Juyal is thanked for the help during the SEM-EDX analysis. Swakangha Ghosh is thanked for her help during fieldwork. This work is part of SC's doctoral thesis on the Sung Valley UACC. We thank the Editor, Prof. Hiroaki Ohfuji, for very efficient editorial handling and Ivan F. Chayka and an anonymous reviewer for the critical reviews, which have greatly improved the quality of the manuscript.

## Author contributions

All authors contributed to conceptualization; SC, KS, and SR curated the data; SC and KS investigated the study; SC and SR contributed to methodology; SC contributed to statistical analysis, figure generation, and writing—original draft; KS and SK contributed to writing—review and editing, supervision, and advice. All authors read and approved the final manuscript.

## Funding

This research received no specific grant from any funding agency in the public, commercial, or not-for-profit sectors.

## Availability of data and materials

The dataset supporting the conclusions of this article is included within the article.

## Competing interests

The authors declare that they have no competing interest.

## Author details

<sup>1</sup>Wadia Institute of Himalayan Geology, 33, GMS Road, Dehradun 248001, India. <sup>2</sup>Department of Geology, Centre of Advanced Study, Kumaun University, Nainital, India.

Received: 18 January 2022 Accepted: 1 December 2022

Published online: 19 December 2022

## References

- Anderson AT Jr (1979) Water in some hypersthene magmas. *J Geol* 87:509–531
- Anderson AT, Samson I, Anderson A, Marshall D (2003) An introduction to melt (glass±crystals) inclusions. Fluid inclusions, analysis and interpretation. Mineralogical Association of Canada, Ottawa, Short Course, vol 32, pp 353–364
- Andreeva IA, Kovalenko VI, Nikiforov AV, Kononkova NN (2007) Compositions of magmas, formation conditions, and genesis of carbonate-bearing jiolites and carbonatites of the Belaya Zima alkaline carbonatite complex, Eastern Sayan. *Petrology* 15(6):551–574
- Armienti P, Pareschi MT, Innocenti F, Pompilio M (1994) Effects of magma storage and ascent on the kinetics of crystal growth. *Contrib Mineral Petrol* 115(4):402–414
- Bataleva Y, Palyanov Y, Borzdov Y (2018) Sulfide formation as a result of sulfate subduction into silicate mantle (experimental modeling under high P, T-parameters). *Minerals* 8(9):373
- Beccaluva L, Bianchini G, Natali C, Siena F (2017) The alkaline-carbonatite complex of Jacupiranga (Brazil): magma genesis and mode of emplacement. *Gondwana Res* 44:157–177
- Bell K, Kjarsgaard BA, Simonetti A (1998) Carbonatites—into the twenty-first century. *J Petrol* 39(11–12):1839–1845
- Berkesi M, Bali E, Bodnar RJ, Szabó Á, Guzmics T (2020) Carbonatite and highly peralkaline nephelinite melts from Oldoinyo Lengai Volcano, Tanzania: the role of natrite-normative fluid degassing. *Gondwana Res* 85:76–83
- Brooker RA, Kjarsgaard BA (2011) Silicate-carbonate liquid immiscibility and phase relations in the system  $SiO_2$ - $Na_2O$ - $Al_2O_3$ - $CaO$ - $CO_2$  at 0.1–2.5 GPa with applications to carbonatite genesis. *J Petrol* 52:1281–1305
- Cashman KV, Marsh BD (1988) Crystal size distribution (CSD) in rocks and the kinetics and dynamics of crystallization II, Makaopuhi lava lake. *Contrib Mineral Petrol* 99:292–305
- Chayka IF, Kamenetsky VS, Zhitova LM, Izokh AE, Tolstykh ND, Abersteiner A, Lobastov BM, Yakich TY (2020) Hybrid nature of the platinum group element chromite-rich rocks of the Norilsk 1 intrusion: Genetic constraints from Cr spinel and spinel-hosted multiphase inclusions. *Econ Geol* 115(6):1321–1342
- Chayka IF, Kamenetsky VS, Vladykin NV, Kontonikas-Charos A, Prokopyev IR, Stepanov SY, Krashennnikov SP (2021) Origin of alkali-rich volcanic and alkali-poor intrusive carbonatites from a common parental magma. *Sci Rep* 11(1):1–13
- Chen W, Kamenetsky VS, Simonetti A (2013) Evidence for the alkaline nature of parental carbonatite melts at Oka complex in Canada. *Nat Commun* 4(1):1–6
- Chmyz L, Arnaud N, Biondi JC, Azzone RG, Bosch D, Ruberti E (2017) Ar–Ar ages, Sr–Nd isotope geochemistry, and implications for the origin of the silicate rocks of the Jacupiranga ultramafic-alkaline complex (Brazil). *J S Am Earth Sci* 77:286–309
- Choudhary S, Sen K, Kumar S, Rana S, Ghosh S (2021) Forsterite reprecipitation and carbon dioxide entrapment in the lithospheric mantle during its interaction with carbonatitic melt: a case study from the Sung Valley ultramafic–alkaline–carbonatite complex, Meghalaya. *NE India Geol Mag* 158(3):475–486
- Choudhary S, Sen K, Kumar S (2022) Pyroxenite hosted chalcopyrites from Sung valley, Meghalaya, NE India: Implications for formation of both high- and low-temperature sulphides in plume derived magma. *Geol Soc Spec Publ* 518(1):575–591
- Church AA (1996) The petrology of the Kerimasi carbonatite volcano and the carbonatites of Oldoinyo Lengai with a review of other occurrences of extrusive carbonatites. University of London, University College London (United Kingdom)
- Danyushevsky LV, McNeill AW, Sobolev AV (2002) Experimental and petrological studies of melt inclusions in phenocrysts from mantle-derived magmas: an overview of techniques, advantages and complications. *Chem Geol* 183:5–24
- Das S, Basu AR, Mukherjee BK (2017) In situ peridotitic diamond in Indus ophiolite sourced from hydrocarbon fluids in the mantle transition zone. *Geology* 45(8):755–758
- Downes H, Kostoula T, Jones AP, Thirlwall MF (2002) Geochemistry and Sr–Nd isotope composition of peridotite xenoliths from Monte Vulture, south central Italy. *Contrib Mineral Petrol* 144:78–92
- Eberl DD, Kile DE, Drits VA (2002) On geological interpretations of crystal size distributions: constant vs. proportionate growth. *Am Min* 87:1235–1241
- Faure F, Tissandier L (2014) Contrasted liquid lines of descent revealed by olivine-hosted melt inclusions and the external magma. *J Petrol* 55(9):1779–1798
- Freestone IC, Hamilton DL (1980) The role of liquid immiscibility in the genesis of carbonatites—an experimental study. *Contrib Mineral Petrol* 73(2):105–117
- Frezzotti ML (2001) Silicate-melt inclusions in magmatic rocks: applications to petrology. *Lithos* 55:273–299
- Frezzotti ML, Tecce F, Casagli A (2012) Raman spectroscopy for fluid inclusion analysis. *J Geochem Explor* 112:1–20
- Giuliani A, Kamenetsky VS, Phillips D, Kendrick MA, Wyatt BA, Goemann K (2012) Nature of alkali-carbonate fluids in the sub-continental lithospheric mantle. *Geology* 40:967–970



- Golovin AV, Sharygin IS, Kamenetsky VS, Korsakov AV, Yaxley GM (2018) Alkali-carbonate melts from the base of cratonic lithospheric mantle: links to kimberlites. *Chem Geol* 483:261–274
- Golovin AV, Sharygin IS, Korsakov AV, Kamenetsky VS, Abersteiner A (2020) Can primitive kimberlite melts be alkali-carbonate liquids: composition of the melt snapshots preserved in deepest mantle xenoliths. *J Raman Spectrosc* 51(9):1849–1867
- Gomes CB, Ruberti E, Comin-Chiaramonti P, Azzone RG (2011) Alkaline magmatism in the Ponta Grossa Arch, SE Brazil: a review. *J S Am Earth Sci* 32:152–168
- Gupta RP, Sen AK (1988) Imprints of ninety-east ridge in the shillong plateau, Indian Shield. *Tectonophysics* 154:335–341
- Guzmics T, Kodolányi J, Kovács I, Szabó C, Bali E, Ntaflós T (2008) Primary carbonatite melt inclusions in apatite and in K-feldspar of clinopyroxene-rich mantle xenoliths hosted in lamprophyre dikes (Hungary). *Mineral Petrol* 94(3):225–242
- Guzmics T, Mitchell RH, Berkesi M, Szabo C (2009) Carbonatite melt inclusions in coexisting magnetite, apatite and monticellite from Kerimasi carbonatite, Tanzania. *Geochim Cosmochim Acta Supplement* 73:A483
- Guzmics T, Mitchell RH, Szabó C, Berkesi M, Milke R, Abart R (2011) Carbonatite melt inclusions in coexisting magnetite, apatite and monticellite in Kerimasi calcicarbonatite, Tanzania: melt evolution and petrogenesis. *Contrib Mineral Petrol* 161:177–196
- Guzmics T, Mitchell RH, Szabó C, Berkesi M, Milke R, Ratter K (2012) Liquid immiscibility between silicate, carbonate and sulfide melts in melt inclusions hosted in coprecipitated minerals from Kerimasi volcano (Tanzania): evolution of carbonated nephelinitic magma. *Contrib Mineral Petrol* 164:101–122
- Halama R, Vennemann T, Siebel W, Markl G (2005) The Grønødal-Ika carbonatite-syenite complex, South Greenland: carbonatite formation by liquid immiscibility. *J Petrol* 46(1):191–217
- Hamilton DL, Bedson P, Esson J (1989) The behaviour of trace elements in the evolution of carbonatites. In: Bell K (ed) *Carbonatite—Genesis and Evolution*. Unwin Hyman, London, pp 405–427
- Higgins MD (1996) Magma dynamics beneath Kameni volcano, Thera, Greece, as revealed by crystal size and shape measurements. *J Volcanol Geotherm Res* 70(1–2):37–48
- Higgins MD (2000) Measurement of crystal size distributions. *Am Mineral* 85:1105–1116
- Higgins MD (2002) Closure in crystal size distributions (CSD), verification of CSD calculations, and the significance of CSD fans. *Am Mineral* 87(1):171–175
- Higgins MD (2011) Textural coarsening in igneous rocks. *Int Geol Rev* 53(3–4):354–376
- Inanli FO, Huff WD (2009) Quartz crystal size distribution of the Ordovician Millbrig K-bentonite. *J Volcanol Geotherm Res* 184(3–4):285–291
- Jaeger JC (1968) Cooling and solidification of igneous rocks. In: Hess HH, Poldervaart A (ed) *Basalts: the poldervaart treatise on rocks of basaltic composition*, vol 2. John Wiley and Sons, New York, pp 503–536
- Jones AP, Kostoula T, Stoppa F, Woolley AR (2000) Petrography and mineral chemistry of mantle xenoliths in a carbonate-rich mellilitic tuff from Mt. Vulture volcano, southern Italy. *Mineral Mag* 64(4):593–613
- Jones AP, Genge M, Carmody L (2013) Carbonate melts and carbonatites. *Rev Mineral Geochem* 75(1):289–322
- Káldos R, Guzmics T, Mitchell RH, Dawson JB, Milke R, Szabó C (2015) A melt evolution model for Kerimasi volcano, Tanzania: Evidence from carbonate melt inclusions in jacupirangite. *Lithos* 238:101–119
- Kamacı Ö, Altunkaynak Ş (2019) Magma chamber processes and dynamics beneath northwestern Anatolia: Insights from mineral chemistry and crystal size distributions (CSDs) of the Kepsut volcanic complex (NW Turkey). *J Asian Earth Sci* 181:103889
- Kamenetsky VS, Kamenetsky MB (2010) Magmatic fluids immiscible with silicate melts: examples from inclusions in phenocrysts and glasses, and implications for magma evolution and metal transport. *Geofluids* 10:293–311
- Kamenetsky VS, Golovin AV, Maas R, Giuliani A, Kamenetsky MB, Weiss Y (2014) Towards a new model for kimberlite petrogenesis: evidence from unaltered kimberlites and mantle minerals. *Earth-Sci Rev* 139:145–167
- Kjarsgaard BA, Hamilton DL (1988) Liquid immiscibility and the origin of alkali-poor carbonatites. *Mineral Mag* 52(364):43–55
- Klein J, Mueller SP, Helo C, Schweitzer S, Gurioli L, Castro JM (2018) An expanded model and application of the combined effect of crystal-size distribution and crystal shape on the relative viscosity of magmas. *J Volcanol Geotherm Res* 357:128–133
- Korobeinikov AN, Mitrofanov FP, Gehör S, Laajoki K, Pavlov VP, Mamontov VP (1998) Geology and copper sulphide mineralization of the Salmagorskii ring igneous complex, Kola Peninsula, NW Russia. *J Petrol* 39(11–12):2033–2041
- Kowallis BJ, Christiansen EH, Dorais MJ, Winkel A, Henze P, Franzen L, Mosher H (2022) Variation of Fe, Al, and F Substitution in Titanite (Sphene). *Geosciences* 12(6):229
- Le Bas MJ (1981) Carbonatite magmas. *Mineral Mag* 44(334):133–140
- Lee WJ, Wyllie PJ (1994) Experimental data bearing on liquid immiscibility, crystal fractionation, and the origin of calcicarbonatites and natrocarbonatites. *Int Geol Rev* 36(9):797–819
- Marsh BD (1988) Crystal size distribution (CSD) in rocks and the kinetics and dynamics of crystallization. *Contrib Mineral Petrol* 99:277–291
- Marsh BD (1998) On the interpretation of crystal size distributions in magmatic systems. *J Petrol* 39(4):553–599
- Mathez EA (1995) Magmatic metasomatism and formation of the Merensky reef, Bushveld Complex. *Contrib Mineral Petrol* 119(2):277–286
- Melluso L, Srivastava RK, Guarino V, Zanetti A, Sinha AK (2010) Mineral compositions and petrogenetic evolution of the ultramafic-alkaline-carbonatite complex of Sung Valley Northeastern India. *Canad Mineral* 48(1):205–229
- Mitchell RH (1980) Pyroxenes of the Fen alkaline complex. *Norway Am Min* 65(1–2):45–54
- Mitchell RH (2009) Peralkaline nephelinite–natrocarbonatite immiscibility and carbonatite assimilation at Oldoinyo Lengai, Tanzania. *Contrib Mineral Petrol* 158:589–598
- Mitchell RH, Dawson JB (2012) Carbonate-silicate immiscibility and extremely peralkaline silicate glasses from Nasira cone and recent eruptions at Oldoinyo Lengai volcano, Tanzania. *Lithos* 152:40–46
- Moine BN, Grégoirec M, O'Reilly SY, Delpech G, Sheppard SMF, Lorand JP, Renac C, Giret A, Cottin JY (2004) Carbonatite melt in oceanic upper mantle beneath the Kerguelen Archipelago. *Lithos* 75:239–252
- Morgan DJ, Jerram DA, Chertkoff DG, Davidson JP, Pearson DG, Kronz A, Nowell GM (2007) Combining CSD and isotopic microanalysis: magma supply and mixing processes at Stromboli Volcano, Aeolian Islands, Italy. *Earth Planet Sci Lett* 260:419–431
- Morimoto N, Fabries J, Ferguson AK, Ginzburg IV, Ross M, Seifert FA, Zussman J, Aoki K, Gottardi D (1988) Nomenclature of Pyroxenes. *Am Mineral* 62:53–62
- Nadeau O, Stevenson R, Jébrak M (2016) Evolution of Montviel alkaline-carbonatite complex by coupled fractional crystallization, fluid mixing and metasomatism—part I: petrography and geochemistry of metasomatic aegirine-augite and biotite: Implications for REE–Nb mineralization. *Ore Geol Rev* 72:1143–1162
- Nielsen TFD (1980) The petrology of a melilitolite, melteigite, carbonatite and syenite ring dike system in the Gardiner complex, East Greenland. *Lithos* 13:181–197
- Nielsen TF, Veksler IV (2002) Is natrocarbonatite a cognate fluid condensate? *Contrib Mineral Petrol* 142(4):425–435
- Nielsen TFD, Solovova IP, Veksler IV (1997) Parental melts of melilitolite and origin of alkaline carbonatite: evidence from crystallised melt inclusions, gardiner complex. *Contrib Mineral Petrol* 126(4):331–344
- Panina LI, Motorina IV (2008) Liquid immiscibility in deep-seated magmas and the generation of carbonatite melts. *Geochem Int* 46:448–464
- Ray JS, Pande K (2001) <sup>40</sup>Ar–<sup>39</sup>Ar age of carbonatite-alkaline magmatism in Sung Valley Meghalaya, India. *J Asian Earth Sci* 110:185–190
- Ray JS, Ramesh R, Pande K (1999) Carbon isotopes in Kerguelen plume-derived carbonatites: evidence for recycled inorganic carbon. *Earth Planet Sci Lett* 170:205–214
- Ray JS, Trivedi JR, Dayal AM (2000) Strontium isotope systematics of Amba Dongar and Sung Valley carbonatite-alkaline complexes, India: evidence for liquid immiscibility, crustal contamination and long-lived Rb=Sr enriched mantle source. *J Asian Earth Sci* 18:585–594
- Roedder E (1979) Origin and significance of magmatic inclusions. *Bull Mineral* 102:487–510
- Roedder E (1972) U. S. G. S. prof. Pap., 440 JJ.

- Savard JJ, Mitchell RH (2021) Petrology of ijolite series rocks from the Prairie Lake (Canada) and Fen (Norway) alkaline rock-carbonatite complexes. *Lithos*, pp. 106–188.
- Seifert W, Thomas R (1995) Silicate-carbonate immiscibility: a melt inclusion study of olivine melilitite and wehrlite xenoliths in tephrite from the Elbe Zone, Germany. *Chem Erde* 55:263–280
- Sekisova VS, Sharygin VV, Zaitsev AN, Strekopytov S (2015) Liquid immiscibility during crystallization of forsterite-phlogopite ijolites at Oldoinyo Lengai volcano, Tanzania: study of melt inclusions. *Russ Geol Geophys* 56(12):1717–1737
- Sen AK (1999) Origin of the Sung Valley carbonatite complex, Meghalaya, India: major element geochemistry constraints. *J. Geol. Soc. India*
- Sharygin VV, Kamenetsky VS, Zaitsev AN, Kamenetsky MB (2012) Silicate–natrocarbonatite liquid immiscibility in 1917 eruption combeite–wollastonite nephelinite, Oldoinyo Lengai Volcano, Tanzania: Melt inclusion study. *Lithos* 152:23–39
- Shastri A, Kumar S (1996) Trace and rare earth elements geochemistry of alkaline rocks of Sarnu-Dandali, Harmer. Rajasthan. *J Geol Soc India* 48(6):663–670
- Sobolev AV (1996) Melt inclusions in minerals as a source of principal petrologic information. *Petrologiya* 4:228–239
- Sokolov SV, Veksler IV, Senin VG (1999) Alkalis in carbonatite magmas: new evidence from melt inclusions. *Petrology* 7:602–609
- Srivastava RK (2020) Early Cretaceous alkaline/ultra-alkaline silicate and carbonatite magmatism in the Indian Shield—a review: implications for a possible remnant of the Greater Kerguelen Large Igneous Province. *Episodes J Int Geosci* 43:300–311
- Srivastava RK, Sinha AK (2004) Early Cretaceous Sung Valley ultramafic-alkaline-carbonatite complex Shillong Plateau, Northeastern India: petrological and genetic significance. *Mineral Petrol* 80(3–4):241–263
- Srivastava RK, Heaman LM, Sinha AK, Shihua S (2005) Emplacement age and isotope geochemistry of Sung Valley alkaline-carbonatite complex, Shillong Plateau, northeastern India: Implications for primary carbonate melt and genesis of the associated silicate rocks. *Lithos* 81(1–4):33–54
- Srivastava RK, Guarino V, Wu FY, Melluso L, Sinha AK (2019) Evidence of sub-continental lithospheric mantle sources and open-system crystallization processes from in-situ U-Pb ages and Nd–Sr–Hf isotope geochemistry of the Cretaceous ultramafic-alkaline (carbonatite) intrusions from the Shillong Plateau, North-Eastern India. *Lithos* 330:108–119
- Stoppa F, Schiazza M, Rosatelli G, Castorina F, Sharygin VV, Ambrosio FA, Vicentini N (2019) Italian carbonatite system: from mantle to ore-deposit. *Ore Geol Rev* 114:103041
- Taubald H, Morteani G, Satir M (2004) Geochemical and isotopic (Sr, C, O) data from the alkaline complex of Grønneidal-Ika (South Greenland): evidence for unmixing and crustal contamination. *Int J Earth Sci* 93:348–360
- Thompson AB, Aerts M, Hack AC (2007) Liquid immiscibility in silicate melts and related systems. *Rev Mineral Geochem* 65:99–127
- Thompson J, Wiens R, Sharma S, Lucey P, Misra A (2005) Combined remote LIBS and Raman spectroscopy measurements: Lunar and Planetary Science XXXVI pdf, 1517.
- Ulmer P, Sweeney RJ (2002) Generation and differentiation of group II kimberlites: constraints from a high-pressure experimental study to 10 GPa. *Geochim Cosmochim Acta* 66(12):2139–2153
- Veena K, Pandey BK, Krishnamurthy P, Gupta JN (1998) Pb, Sr and Nd isotopic systematics of the carbonatites of Sung Valley, Meghalaya, Northeast India: implications for contemporary plume-related mantle source characteristics. *J Petrol* 39:1875–1884
- Veksler IV, Petibon C, Jenner GA, Dorfman AM, Dingwell DB (1998) Trace element partitioning in immiscible silicate–carbonate liquid systems: an initial experimental study using a centrifuge autoclave. *J Petrol* 39:2095–2104
- Verwoerd WJ (1978) Liquid immiscibility and the carbonatite–ijolite relationship: preliminary data on the join  $\text{NaFe}_3\text{Si}_2\text{O}_6\text{–CaCO}_3$  and related compositions. *Carnegie Institute Washington, Yearbook*, 77
- Viladkar SG, Schleicher H, Pawaskar P (1994) Mineralogy and geochemistry of the Sung Valley carbonatite complex, Shillong, Meghalaya, India. *Njb Mineral MhH* 11:499–517
- Wang D, Liu J, Carranza EJM, Zhai D, Wang Y, Zhen S, Wang J, Wang J, Liu Z, Zhang F (2019) Formation and evolution of snowball quartz phenocrysts in the Dongping porphyritic granite, Hebei Province, China: insights from fluid inclusions, cathodoluminescence, trace elements, and crystal size distribution study. *Lithos* 340:239–254
- Watkinson DH, Wyllie PJ (1971) Experimental study of the composition join  $\text{NaAlSi}_3\text{O}_8\text{–CaCO}_3\text{–H}_2\text{O}$  and the genesis of Alkaline Rock—Carbonatite Complexes. *J Petrol* 12(2):357–378
- Winter JD (2001) An introduction to igneous and metamorphic petrology: Prentice Hall, New Jersey
- Woolley AR, Bailey DK (2012) The crucial role of lithospheric structure in the generation and release of carbonatites: geological evidence. *Mineral Mag* 76:259–270
- Xu C, Zhang H, Huang Z, Liu C, Qi L, Li W, Guan T (2004) Genesis of the carbonatite syenite complex and REE deposit at Maoniuping, Sichuan Province, China: evidence from Pb isotope geochemistry. *Geochem J* 38:67–76
- Yaxley GM, Kjarsgaard BA, Jaques AL (2021) Evolution of carbonatite magmas in the upper mantle and crust. *Elements* 17(5):315–320
- Yaxley GM, Anenburg M, Tappe S, Decree S, Guzmics T (2022) Carbonatites: classification, sources, evolution, and emplacement. *Annu Rev Earth Planet Sci*
- Zaitsev AN, Keller J (2006) Mineralogical and chemical transformation of Oldoinyo Lengai natrocarbonatites. *Tanzania Lithos* 91(1–4):191–207
- Zhou JL, Li XH, Tang GQ, Gao BY, Bao ZA, Ling XX, Wu LG, Lu K, Zhu YS, Liao X (2018) Ca. 890 Ma magmatism in the northwest Yangtze block, South China: SIMS U-Pb dating, in-situ Hf–O isotopes, and tectonic implications. *J Asian Earth Sci* 151:101–111

## Publisher's Note

Springer Nature remains neutral with regard to jurisdictional claims in published maps and institutional affiliations.

Submit your manuscript to a SpringerOpen® journal and benefit from:

- Convenient online submission
- Rigorous peer review
- Open access: articles freely available online
- High visibility within the field
- Retaining the copyright to your article

Submit your next manuscript at ► [springeropen.com](https://www.springeropen.com)